

Shell element formulation of multi-step inverse analysis for axisymmetric deep drawing process

Choongho Lee and Jian Cao*

Department of Mechanical Engineering, Northwestern University, Evanston, IL 60208, U.S.A.

SUMMARY

Inverse analysis today is generally performed with membrane models in analysing sheet metal forming processes. Given the final desired configuration, it usually estimates the deformation in a one-step calculation. However, for some practical problems where the bending effect is significant and the strain history departs from a linear path, this calculation becomes not good enough to provide the optimal design values. In this paper, an axisymmetric shell element for the multi-step inverse analysis is developed for more accurate prediction of design variables such as the initial blank shape, strain distributions, and intermediate shapes, etc. The algorithm has been applied to deep drawing processes for both thin and relatively thick sheet metal. Numerical examples demonstrate that the proposed combination of shell element and multi-step inverse analysis can provide more precise results than the previous algorithms used in inverse analysis. Copyright © 2001 John Wiley & Sons, Ltd.

KEY WORDS: multi-step inverse analysis; axisymmetric shell element; bending and unbending effect; deep drawing; blank design

1. INTRODUCTION

In the design of deep drawing processes, many process parameters, e.g. die geometry, initial blank shape, blank holding force, and lubrication, need to be determined. It is critical to the industry that these design variables are optimized for one particular forming process. The design process has traditionally relied on experience and intuition accompanied in many cases by physical trial and error approach. With the development of computer technology, numerical simulations using, for example, incremental finite element methods (FEM) have been developed. However, the majority of the applications using finite element methods has been deterministic, in which a set of design parameters is given and simulation results are interpreted by users. Additional simulations need to be performed if the results are not satisfactory. The determination of those design parameters is

*Correspondence to: Jian Cao, Department of Mechanical Engineering, Northwestern University, 2145 Sheridan Road, Evanston, IL 60208, U.S.A.

†E-mail: jcao@nwu.edu

Contract/grant sponsor: NSF; contract/grant number DMI-9703249

Contract/grant sponsor: KOSEF (Korea Science and Engineering Foundation)

again mainly based on users' experience and interpretation. Such design process usually requires enormous amount of time and cost to determine the optimal process parameters.

The desire of having computer programs to automatically determine the optimal tooling and process parameters has attracted many researchers. The attempts can be classified into two categories, forward analysis and inverse analysis. In the forward analysis, sensitivity analysis for incremental FEM has been widely studied. The approach is to calculate the gradient of the objective function and to study the effects of process parameters on the states of the final product. Since metal forming processes are generally highly non-linear and history dependent, many researchers have used the direct differentiation method for the calculation of sensitivity [1–7]. Badrinarayanan and Zabaraz [1, 2] calculated the differentiation terms directly from the weak form of equilibrium equations and demonstrated the approach on determining a preform shape of an upsetting problem and a die profile of an extrusion problem. Alternatively, the differential terms can be derived from the finite element discretized weak form as described in Chenot and co-workers [3–5]. They calculated a preform shape of an upsetting problem and tool shapes of a two-step forging problem. Zhao and colleagues [6, 7] developed a similar optimization scheme to that of Chenot and co-workers. They focused on the optimal design of die shapes of performs rather than that of preform shapes. Kleiber *et al.* [8, 9] derived sensitivity equations by both the direct differentiation method and the adjoint variable method. Joun and Hwang [10] used the adjoint variable method to optimize the die profile of a three-dimensional steady-state extrusion problem. Most sensitivity analyses for incremental FEM have been applied to simple two-dimensional problems such as upsetting, forging, and extrusion. However, there is very little practical application to sheet metal forming processes and many difficulties still remain in the implementation of sensitivity analysis to practical and complex bulk forming problems.

Another promising method to determine the optimal binder force trajectory in the forward mode was presented in Cao and Boyce [11] for a given initial blank geometry and tooling geometry. A user-defined element serves the purpose of closed-loop control in the FEM simulation. This element senses the current wrinkling and tearing tendencies and alters the binder force so that no excessive wrinkles are present. The optimal binder force history was determined in one run of the FEM simulation.

An alternative approach for design optimization is the inverse analysis (IA), where the final part geometry and tooling geometry are given, but the initial blank geometry and forming process parameters are not provided. The initial attempt was made by Jimma [12], Hazek and Lange [13], and Karima [14] using the slip line field method. In their work, elements of the deformed part were traced back to their original configurations assuming plane strain deformation. Later, Vogel and Lee [15], and Chen and Sowerby [16] solved problems considering plane stress deformation. However, these two methods have been applied only to cups with a flat end. Sowerby *et al.* [17] and Blount and Stevens [18] developed the geometric mapping method. It unfolds a three-dimensional shape into a flat surface using a simple algorithm without considering the deformation of the sheet.

With the ability to incorporate material deformation behaviour, the inverse finite element analysis (IA) using the deformation theory has been developed to meet the needs of the design community. However, most inverse problems are ill-posed, they tend to be more difficult to solve than direct problems. The existence, uniqueness and stability of the solutions of ill-posed problems are not guaranteed [19]. To overcome this issue, *a priori* information on the required solution is often introduced in the form of constraints. Even though it is not easy to solve inverse problems, inverse formulation has many advantages in the design process. Levy *et al.* [20] calculated the

initial blank size of axisymmetric problems using three-node quadratic membrane elements. After Levy *et al.*'s work, the one-step inverse analysis using membrane elements (IA-membrane) was studied by Majlessi and Lee [21], Batoz and co-workers [22], Chung and Richmond [23–25], Liu and Karima [26], Liu and Assempoor [27], and Lee and Huh [28]. This approach is good for general sheet metal forming processes. However, due to the absence of bending stiffness and the use of the deformation theory, the amount of error introduced increases as the deformation path becomes more non-linear and the ratio of sheet thickness to bending radius increases. The multi-step IA-membrane approach, which divides the forming into smaller forming steps, increases the prediction accuracy as evident in Majlessi and Lee [29] for axisymmetric problems and Lee and Huh [30] for simple three-dimensional problems. However, it is not helpful when bending is important. To address the bending issue, Batoz and co-workers [31, 32] derived a shell element formulation for one-step inverse analysis without the rotational degree of freedom at the nodal points.

In this paper, an axisymmetric shell element for the multi-step inverse analysis (IA) is derived for more accurate calculation of strain and the initial blank shape. The shell element for the multi-step IA is formulated in Section 2 aiming at providing reasonable results for both relatively thick and thin sheet drawing. Sections 3 and 4 describe the formulae of the employed constitutive law and key matrices in the inverse analysis, respectively. As the number of analysis steps increases following the procedure illustrated in Section 5, the bending and unbending effect can be considered more accurately. Comparisons among the inverse analysis using the present algorithm (IA-Shell), the existing inverse analysis methodology (IA-membrane) and the forward FEM simulation are given in Section 6. Numerical examples show that the new algorithm can provide more accurate results than the previous algorithms used in the inverse analysis. With this improvement, the proposed algorithm, combined with an optimization scheme, could be used to determine other process parameters such as tooling geometry for complex forming problems.

2. KINEMATICS OF AXISYMMETRIC SHELL FOR INVERSE ANALYSIS

The development of shell elements in the incremental forward analysis was summarized and reviewed in References [33, 34]. The major milestones include, but are not limited to, the degenerated shell approach, stress-resultant-based formulations and Cosserat surface approach, reduced integration techniques with stabilization (hourglass control), incompatible modes approach, enhanced strain formulations (mixed and hybrid formulations), elements based on the 3-D elasticity theory, co-rotational approaches, and higher-order theories for composites. On the other hand, only a few papers with shell element formulation are founded in the inverse analysis. Batoz and co-workers [31, 32] derived an inverse formulation using a simple discrete Kirchhoff triangular (DKT) shell element for taking into account the bending effect. However, the ability of their shell element is limited due to the lack of the rotational degrees of freedom in the formulation and one-step inverse analysis was performed without considering intermediate deformed states.

As to our best knowledge, no axisymmetric shell element has been developed for multi-step inverse analysis. Here, we adopt basic concepts of the axisymmetric shell element developed in References [35, 36] as presented in the theory manual of ABAQUS (a commercial finite element package) [37]. The assumptions involved in the shell element are described in the ABAQUS theory manual. The variables of the shell element for incremental forward analysis are the position \mathbf{x} and the rotation ω at time $t = t_0 + \Delta t$ (Figure 1), where ω is the rotation of the thickness direction

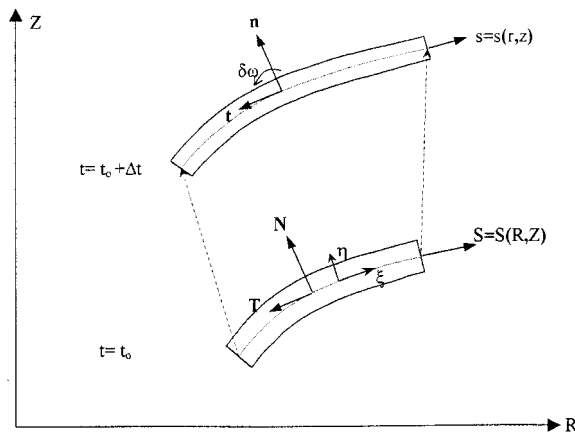


Figure 1. Kinematics of an axisymmetric shell for inverse analysis.

vector \mathbf{n} initially orthogonal to the initial surface. However, the variables for our inverse analysis are the initial position along the meridian surface at time $t = t_0$, $S(\mathbf{X})$, and the rotation ω at time $t = t_0 + \Delta t$. We derived basic equations according to the variable $S(\mathbf{X})$ and ω as follows:

The metric tensors $G_{\alpha\alpha}$, $g_{\alpha\alpha}$ at time $t = t_0$ and $t = t_0 + \Delta t$ are

$$G_{11} = \frac{d\mathbf{X}}{d\xi} \cdot \frac{d\mathbf{X}}{d\xi} \quad G_{22} = R^2 \quad \text{at } t = t_0 \tag{1a}$$

$$g_{11} = \frac{d\mathbf{x}}{d\xi} \cdot \frac{d\mathbf{x}}{d\xi} \quad g_{22} = r^2, \quad \text{at } t = t_0 + \Delta t \tag{1b}$$

The incremental stretch ratio $\Delta\lambda_\alpha$ and the curvature measures $B_{\alpha\alpha}$, $b_{\alpha\alpha}$ are written as

$$\Delta\lambda_1 = \left(\frac{g_{11}}{G_{11}} \right)^{1/2}, \quad \Delta\lambda_2 = \frac{r}{R} \tag{2}$$

$$B_{11} = \frac{d\mathbf{X}}{d\xi} \cdot \frac{d\mathbf{N}}{d\xi}, \quad B_{22} = RN_r, \quad \text{at } t = t_0 \tag{3a}$$

$$b_{11} = \frac{d\mathbf{x}}{d\xi} \cdot \frac{d\mathbf{n}}{d\xi}, \quad b_{22} = rn_r, \quad \text{at } t = t_0 + \Delta t \tag{3b}$$

The relations between the variations of $\mathbf{X}(R, Z)$ and that of S are expressed as

$$\delta\mathbf{X} = \frac{\partial\mathbf{X}}{\partial S} \delta S = \frac{\partial\mathbf{X}}{\partial\xi} \left(\frac{\partial S}{\partial\xi} \right)^{-1} \delta S, \quad \frac{d\delta\mathbf{X}}{d\xi} = \frac{\partial\mathbf{X}}{\partial\xi} \left(\frac{\partial S}{\partial\xi} \right)^{-1} \frac{d\delta S}{d\xi} \tag{4a}$$

$$\delta R = \frac{\partial R}{\partial S} \delta S = \frac{\partial R}{\partial\xi} \left(\frac{\partial S}{\partial\xi} \right)^{-1} \delta S \tag{4b}$$

Then the first variations of Equations (2)–(3) are derived according to the variation of $S(\mathbf{X})$ and ω as

$$\delta\Delta\lambda_1 = -\frac{1}{\Delta\lambda_1} \frac{g_{11}}{G_{11}^2} \frac{d\mathbf{X}}{d\xi} \cdot \frac{d\delta\mathbf{X}}{d\xi} = -\frac{\Delta\lambda_1}{G_{11}} \frac{d\mathbf{X}}{d\xi} \cdot \frac{d\delta\mathbf{X}}{d\xi} = -\Delta\lambda_1 \left(\frac{\partial S}{\partial \xi}\right)^{-1} \frac{d\delta S}{d\xi} \tag{5a}$$

$$\delta\Delta\lambda_2 = -\frac{r}{R^2} \delta R = -\frac{\Delta\lambda_2}{R} \delta R = -\frac{\Delta\lambda_2}{R} \frac{\partial R}{\partial \xi} \left(\frac{\partial S}{\partial \xi}\right)^{-1} \delta S \tag{5b}$$

$$\delta B_{11} = \frac{d\delta\mathbf{X}}{d\xi} \cdot \frac{d\mathbf{N}}{d\xi} = B_{11} \left(\frac{\partial S}{\partial \xi}\right)^{-1} \frac{d\delta S}{d\xi} \tag{6a}$$

$$\delta B_{22} = \delta R N_r = N_r \frac{\partial R}{\partial \xi} \left(\frac{\partial S}{\partial \xi}\right)^{-1} \delta S \tag{6b}$$

$$\delta b_{11} = \frac{d\mathbf{x}}{d\xi} \cdot \mathbf{t} \frac{d\delta\omega}{d\xi} + \frac{d\mathbf{x}}{d\xi} \cdot \frac{d\mathbf{t}}{d\xi} \delta\omega \tag{6c}$$

$$\delta b_{22} = r\delta n_r = r\delta\omega t_r = -r\delta\omega n_z \tag{6d}$$

where

$$\delta\mathbf{n} = \delta\omega\mathbf{t}, \quad \delta\mathbf{t} = -\delta\omega\mathbf{n}, \quad \mathbf{t} = [-n_z \quad n_r] \tag{7}$$

\mathbf{n} rotates according to ω and \mathbf{t} is orthogonal to \mathbf{n} as shown in Figure 1. The second variations for $\Delta\lambda_{\alpha}$, $B_{\alpha\alpha}$ and $b_{\alpha\alpha}$ can be derived as the following:

$$d\delta\Delta\lambda_1 = 2\frac{\Delta\lambda_1}{G_{11}} \frac{d\delta\mathbf{X}}{d\xi} \cdot \frac{d\delta\mathbf{X}}{d\xi} = 2\Delta\lambda_1 \left(\frac{\partial S}{\partial \xi}\right)^{-2} \frac{d\delta S}{d\xi} \frac{d\delta S}{d\xi} \tag{8a}$$

$$d\delta\Delta\lambda_2 = 2\frac{\Delta\lambda_2}{R^2} dR \delta R = 2\frac{\Delta\lambda_2}{R^2} \left(\frac{\partial R}{\partial \xi}\right)^2 \left(\frac{\partial S}{\partial \xi}\right)^{-2} dS \delta S \tag{8b}$$

$$d\delta B_{11} = 0 \tag{9a}$$

$$d\delta B_{22} = 0 \tag{9b}$$

$$\begin{aligned} d\delta b_{11} &= \frac{d\mathbf{x}}{d\xi} \cdot (-d\omega\mathbf{n}) \frac{d\delta\omega}{d\xi} + \frac{d\mathbf{x}}{d\xi} \cdot \frac{d(-d\omega\mathbf{n})}{d\xi} \delta\omega \\ &= -\frac{d\mathbf{x}}{d\xi} \cdot \mathbf{n} \left(\frac{d\delta\omega}{d\xi} d\omega + \frac{d\delta\omega}{d\xi} \delta\omega\right) - \frac{d\mathbf{x}}{d\xi} \cdot \frac{d\mathbf{n}}{d\xi} d\omega \delta\omega \end{aligned} \tag{9c}$$

$$d\delta b_{22} = -r n_r d\omega \delta\omega \tag{9d}$$

The above first and second variations are implemented into finite element equations.

If we assume that the increments of stretch ratios are *not too large* during the increment (i.e. analysis step), the increments of in-plane strains $\Delta\epsilon_{xx}^1$ at any material point can be decomposed

into the following membrane strain $\Delta\varepsilon_{\alpha\alpha}$ and the incremental curvature change measure $\Delta\tilde{\kappa}_{\alpha\alpha}$:

$$\Delta\varepsilon_{\alpha\alpha}^1 \cong \Delta\varepsilon_{\alpha\alpha} + \eta\Delta\tilde{\kappa}_{\alpha\alpha} \tag{10}$$

where

$$\Delta\varepsilon_{\alpha\alpha} = \ln(\Delta\lambda_\alpha) \tag{11}$$

$$\Delta\tilde{\kappa}_{\alpha\alpha} = \frac{\lambda_t^0}{g_{\alpha\alpha}\Delta\lambda_1\Delta\lambda_2}(b_{\alpha\alpha} - \Delta\lambda_\alpha B_{\alpha\alpha}) \tag{12}$$

η in Equation (10) is the natural co-ordinate with respect to the thickness direction and α varies from 1 to 2. If the shell is stretched uniformly, the strain increments must be constant through the thickness direction and the curvature increment should be zero. This requirement can be satisfied by the above modified incremental curvature change measure $\Delta\tilde{\kappa}_{\alpha\alpha}$ [37]. The first variations of strains in Equation (10) can be obtained from Equations (5)–(7).

$$\delta\varepsilon_{11} = \delta \ln(\Delta\lambda_1) = \frac{1}{\Delta\lambda_1} \delta(\Delta\lambda_1) = - \left(\frac{\partial S}{\partial \xi} \right)^{-1} \frac{d\delta S}{d\xi} \tag{13a}$$

$$\delta\varepsilon_{22} = \delta \ln(\Delta\lambda_2) = - \frac{1}{R} \delta R = - \frac{1}{R} \frac{\partial R}{\partial \xi} \left(\frac{\partial S}{\partial \xi} \right)^{-1} \delta S \tag{13b}$$

$$\begin{aligned} \delta\tilde{\kappa}_{\alpha\alpha} &= \delta \left[\frac{\lambda_t^0}{g_{\alpha\alpha}\Delta\lambda_1\Delta\lambda_2}(b_{\alpha\alpha} - \Delta\lambda_\alpha B_{\alpha\alpha}) \right] \\ &= \frac{\lambda_t^0}{g_{\alpha\alpha}\Delta\lambda_1\Delta\lambda_2} \left\{ (b_{\alpha\alpha} - \Delta\lambda_\alpha B_{\alpha\alpha}) \left(\left(\frac{\partial S}{\partial \xi} \right)^{-1} \frac{d\delta S}{d\xi} + \frac{1}{R} \frac{\partial R}{\partial \xi} \left(\frac{\partial S}{\partial \xi} \right)^{-1} \delta S \right) \right. \\ &\quad \left. + (\delta b_{\alpha\alpha} - \delta\Delta\lambda_\alpha B_{\alpha\alpha} - \Delta\lambda_\alpha \delta B_{\alpha\alpha}) \right\} \end{aligned} \tag{14}$$

And the second variations of strains are derived as

$$d\delta\varepsilon_{11} = \frac{2}{G_{11}^2} \frac{d\mathbf{X}}{d\xi} \cdot \frac{d\delta\mathbf{X}}{d\xi} \frac{d\mathbf{X}}{d\xi} \cdot \frac{d\delta\mathbf{X}}{d\xi} - \frac{1}{G_{11}} \frac{d\delta\mathbf{X}}{d\xi} \cdot \frac{d\delta\mathbf{X}}{d\xi} = \left(\frac{\partial S}{\partial \xi} \right)^{-2} \frac{d\delta S}{d\xi} \frac{d\delta S}{d\xi} \tag{15a}$$

$$d\delta\varepsilon_{22} = \frac{1}{R^2} dR \delta R = \frac{1}{R^2} \left(\frac{\partial R}{\partial \xi} \right)^2 \left(\frac{\partial S}{\partial \xi} \right)^{-2} dS \delta S \tag{15b}$$

$$d\delta\tilde{\kappa}_{\alpha\alpha} = d \left[\frac{\lambda_t^0}{g_{\alpha\alpha}\Delta\lambda_1\Delta\lambda_2} \left\{ (b_{\alpha\alpha} - \Delta\lambda_\alpha B_{\alpha\alpha}) \left(\frac{1}{G_{11}} \frac{d\mathbf{X}}{d\xi} \cdot \frac{d\delta\mathbf{X}}{d\xi} + \frac{1}{R} \delta R \right) \right. \right. \\ \left. \left. + (\delta b_{\alpha\alpha} - \delta\Delta\lambda_\alpha B_{\alpha\alpha} - \Delta\lambda_\alpha \delta B_{\alpha\alpha}) \right\} \right]$$

$$= \frac{\lambda_t^0}{g_{\alpha\alpha}\Delta\lambda_1\Delta\lambda_2} \left\{ \begin{aligned} & \left((b_{\alpha\alpha} - \Delta\lambda_\alpha B_{\alpha\alpha}) \left(\left(\frac{\partial S}{\partial \xi} \right)^{-1} \frac{d\delta S}{d\xi} + \frac{1}{R} \frac{\partial R}{\partial \xi} \left(\frac{\partial S}{\partial \xi} \right)^{-1} \delta S \right) \right. \\ & \quad \left. + 2(\delta b_{\alpha\alpha} - \delta\Delta\lambda_\alpha B_{\alpha\alpha} - \Delta\lambda_\alpha \delta B_{\alpha\alpha}) \right) \\ & * \left(\left(\frac{\partial S}{\partial \xi} \right)^{-1} \frac{d\delta S}{d\xi} + \frac{1}{R} \frac{\partial R}{\partial \xi} \left(\frac{\partial S}{\partial \xi} \right)^{-1} \delta S \right) + (b_{\alpha\alpha} - \Delta\lambda_\alpha B_{\alpha\alpha}) \\ & * \left(- \left(\frac{\partial S}{\partial \xi} \right)^{-2} \frac{d\delta S}{d\xi} \frac{d\delta S}{d\xi} - \frac{1}{R^2} \left(\frac{\partial R}{\partial \xi} \right)^2 \left(\frac{\partial S}{\partial \xi} \right)^{-2} dS \delta S \right) \\ & \quad \left. + (d\delta b_{\alpha\alpha} - d\delta\Delta\lambda_\alpha B_{\alpha\alpha} - d\Delta\lambda_\alpha \delta B_{\alpha\alpha}) \right) \end{aligned} \right\} \quad (16)$$

The transverse shear strain is written as

$$\Delta\gamma = \frac{1}{\sqrt{g_{11}}} \frac{d\mathbf{x}}{d\xi} \cdot \mathbf{n} - \frac{1}{\sqrt{G_{11}}} \frac{d\mathbf{X}}{d\xi} \cdot \mathbf{N} \quad (17)$$

and the first and second variations of $\Delta\gamma$ are as follows:

$$\delta\gamma = \frac{1}{\sqrt{g_{11}}} \frac{d\mathbf{x}}{d\xi} \cdot \mathbf{t}\delta\omega + \frac{1}{G_{11}^{3/2}} \frac{d\mathbf{X}}{d\xi} \cdot \frac{d\delta\mathbf{X}}{d\xi} \frac{d\mathbf{X}}{d\xi} \cdot \mathbf{N} - \frac{1}{\sqrt{G_{11}}} \frac{d\delta\mathbf{X}}{d\xi} \cdot \mathbf{N} = \frac{1}{\sqrt{g_{11}}} \frac{d\mathbf{x}}{d\xi} \cdot \mathbf{t}\delta\omega \quad (18)$$

$$d\delta\gamma = d \left[\frac{1}{\sqrt{g_{11}}} \frac{d\mathbf{x}}{d\xi} \cdot \mathbf{t}\delta\omega \right] = - \frac{1}{\sqrt{g_{11}}} \frac{d\mathbf{x}}{d\xi} \cdot \mathbf{n} d\omega \quad (19)$$

3. CONSTITUTIVE EQUATION AND PLASTIC WORK

In a typical deep drawing process, a much larger amount of plastic strain is accumulated in the sheet metal compared to that of elastic strain. As the major concern in the first phase of tooling and process design are the formability issues, sheet material response in the plane of the sheet is assumed to be rigid-plastic following Hill's 2nd-order yield criterion and its associated flow rule. Furthermore, the stress normal to the sheet is assumed to be zero and all the stress states are integrated from the initial state to the final state. Then, the integrated relationship between stress and strain can be expressed as

$$\left\{ \begin{matrix} \sigma_{11} \\ \sigma_{22} \end{matrix} \right\} = \frac{2}{3} \frac{(2+r)(1+r)}{(1+2r)} \frac{\bar{\sigma}}{\Delta\bar{\epsilon}} \begin{bmatrix} 1 & \frac{r}{1+r} \\ \frac{r}{1+r} & 1 \end{bmatrix} \left\{ \begin{matrix} \Delta\epsilon_{11}^1 \\ \Delta\epsilon_{22}^1 \end{matrix} \right\} = \mathbf{D}^{(m)} \Delta\epsilon^1 \quad (20)$$

where

$$\Delta\bar{\epsilon} = \sqrt{\frac{2}{3} \frac{(2+r)(1+r)}{(1+2r)} \left[(\Delta\epsilon_{11}^1)^2 + (\Delta\epsilon_{22}^1)^2 + \frac{2r}{1+r} \Delta\epsilon_{11}^1 \Delta\epsilon_{22}^1 \right]^{1/2}} \quad (21)$$

The above constitutive equation considers normal anisotropy because only axisymmetric problems are considered in this paper. Transverse shears are assumed to be small, and the material response to such deformation is assumed to be linear elastic such as

$$\sigma_s = kG\Delta\gamma = D^{(s)}\Delta\gamma \tag{22}$$

where k is the transverse shear correction factor [38]. Then Equations (20) and (22) can be rewritten together in one matrix equation as

$$\begin{Bmatrix} \sigma_{11} \\ \sigma_{22} \\ \sigma_s \end{Bmatrix} = \begin{bmatrix} \mathbf{D}^{(m)} & \mathbf{0} \\ \mathbf{0} & \mathbf{D}^{(s)} \end{bmatrix} \begin{Bmatrix} \Delta\varepsilon_{11}^1 \\ \Delta\varepsilon_{22}^1 \\ \Delta\gamma \end{Bmatrix} = \mathbf{D}\Delta\varepsilon = \mathbf{D}\mathbf{S}\Delta\mathbf{e} \tag{23}$$

where

$$\Delta\varepsilon = \begin{Bmatrix} \Delta\varepsilon_{11}^1 \\ \Delta\varepsilon_{22}^1 \\ \Delta\gamma \end{Bmatrix} = \begin{bmatrix} 1 & 0 & \eta & 0 & 0 \\ 0 & 1 & 0 & \eta & 0 \\ 0 & 0 & 0 & 0 & 1 \end{bmatrix} \begin{Bmatrix} \Delta\varepsilon_{11} \\ \Delta\varepsilon_{22} \\ \Delta\kappa_{11} \\ \Delta\kappa_{22} \\ \Delta\gamma \end{Bmatrix} = \mathbf{S}\Delta\mathbf{e} \tag{24}$$

Using the above constitutive equation, we can construct the plastic work as

$$W_p(S, \omega) = \int_{\Omega} \sigma\delta\varepsilon \, d\Omega = \int_{\Omega} \Delta\mathbf{e}^T \mathbf{S}^T \mathbf{D}^T \mathbf{S} \delta\Delta\mathbf{e} \, d\Omega = \int_{\Omega_e} \Delta\mathbf{e}^T \hat{\mathbf{D}} \delta\Delta\mathbf{e} 2\pi r J \, d\xi \tag{25}$$

where

$$\hat{\mathbf{D}} = \int_{-0.5}^{0.5} \mathbf{S}^T \mathbf{D}^T \mathbf{S} J_t \, d\eta = \begin{bmatrix} \hat{\mathbf{D}}^{(m)} & \hat{\mathbf{D}}^{(mb)} & \mathbf{0} \\ \hat{\mathbf{D}}^{(mb)} & \hat{\mathbf{D}}^{(b)} & \mathbf{0} \\ \mathbf{0} & \mathbf{0} & \hat{D}^{(s)} \end{bmatrix} \tag{26}$$

$$J = \left| \frac{dS}{d\xi} \right| \text{ meridian direction, } J_t = \left| \frac{dt}{d\eta} \right| \text{ thickness direction} \tag{27}$$

The $\hat{\mathbf{D}}$ of Equation (26) is a constitutive resultant matrix integrated through the thickness direction. The components of matrix $\hat{\mathbf{D}}$ can be expressed separately as

$$\begin{aligned} \hat{\mathbf{D}}^{(m)} &= \int_{-0.5}^{0.5} \mathbf{D}^{(m)} J_t \, d\eta & \hat{\mathbf{D}}^{(mb)} &= \int_{-0.5}^{0.5} \eta \mathbf{D}^{(m)} J_t \, d\eta \\ \hat{\mathbf{D}}^{(b)} &= \int_{-0.5}^{0.5} \eta^2 \mathbf{D}^{(m)} J_t \, d\eta & \hat{D}^{(s)} &= \int_{-0.5}^{0.5} D^{(s)} J_t \, d\eta = \int_{-0.5}^{0.5} kG J_t \, d\eta \end{aligned} \tag{28}$$

where $\hat{\mathbf{D}}^{(m)}$, $\hat{\mathbf{D}}^{(mb)}$, $\hat{\mathbf{D}}^{(b)}$, $\hat{D}^{(s)}$ are the constitutive resultant matrices for membrane, membrane-bending coupling, bending and shear effects, respectively. Then, the plastic work of Equation (25)

can be partitioned in terms of membrane, membrane bending, bending and shear.

$$\begin{aligned}
 W_p(S, \omega) = & \int_{\Omega_e} \Delta \varepsilon^T \hat{\mathbf{D}}^{(m)} \delta \Delta \varepsilon 2\pi r J \, d\xi + \int_{\Omega_e} \Delta \varepsilon^T \hat{\mathbf{D}}^{(mb)} \delta \Delta \kappa 2\pi r J \, d\xi \\
 & + \int_{\Omega_e} \Delta \kappa^T \hat{\mathbf{D}}^{(mb)} \delta \Delta \varepsilon 2\pi r J \, d\xi + \int_{\Omega_e} \Delta \kappa^T \hat{\mathbf{D}}^{(b)} \delta \Delta \kappa 2\pi r J \, d\xi + \int_{\Omega_e} \Delta \gamma^T \hat{\mathbf{D}}^{(s)} \delta \Delta \gamma 2\pi r J \, d\xi
 \end{aligned} \tag{29}$$

The above separation of the plastic work and the conversion of volume integration into the thickness and surface integration can be found in the literatures about the continuum-based resultant shell formulation [39, 40].

4. MINIMIZATION OF POTENTIAL ENERGY

The concept of force equilibrium and the principle of virtual work enable the calculation of the so-called equivalent external work. The plastic potential energy can be expressed as the difference between the internal plastic work and the external work as the following:

$$\Psi(S, \omega) = W_p(S, \omega) - W_e(S, \omega) = \int_{\Omega_e} \Delta \mathbf{e}^T \hat{\mathbf{D}} \delta \Delta \mathbf{e} 2\pi r J \, d\xi - \int_{\partial\Omega_e} \mathbf{t} \delta \mathbf{v} 2\pi r J \, d\xi \tag{30}$$

The friction force and the blank holding force induce the external work $W_e(S, \omega)$. The reaction force \mathbf{t} can be obtained from the derivation of the plastic work by position \mathbf{x} at the final state for the membrane element [41]. In the case of the shell element, the reaction force is derived in Appendix A. In Equation (30) \mathbf{v} is the relative displacement from the initial co-ordinate \mathbf{X} to the final coordinate \mathbf{x} .

$$\mathbf{v}(\mathbf{X}(S)) = [(\mathbf{x} - \mathbf{X} - \mathbf{U}_p) - (\mathbf{N} \cdot (\mathbf{x} - \mathbf{X} - \mathbf{U}_p))\mathbf{N}] \tag{31}$$

where \mathbf{N} is the unit normal vector at the initial co-ordinate and \mathbf{U}_p is the punch displacement for each analysis step. The local minimum of $\Psi(S, \omega)$ corresponds to the possible solution in the inverse analysis and this can be satisfied when the first derivative of $\Psi(S, \omega)$ has a stationary value. The first derivative is expressed as follows:

$$\min \Psi(S, \omega) \Rightarrow \mathbf{R}(\mathbf{U}) \equiv \frac{\partial \Psi}{\partial \mathbf{U}} = \mathbf{0}, \quad \mathbf{U} = \{S, \omega\} \tag{32}$$

where

$$\mathbf{R}(\mathbf{U}) = \int_{\Omega_e} \Delta \mathbf{e}^T \hat{\mathbf{D}} \frac{\partial \Delta \mathbf{e}}{\partial \mathbf{U}} 2\pi r J \, d\xi - \int_{\partial\Omega_e} \mathbf{t} \frac{\partial \mathbf{v}}{\partial \mathbf{U}} 2\pi r J \, d\xi \tag{33}$$

Note that the inverse analysis using Equation (32) might have multiple solutions when deformations are sufficiently large. Chung and Richmond [23, 24] showed a case of multiple solutions in their work. In the case of multiple solutions, the best solution can be selected using the knowledge of forming conditions. For example, in the case where strain concentration is undesired due to its

potential for failure, the solution of the relatively maximum potential energy is desirable since it corresponds to the most evenly distributed deformation among the multiple solutions.

The minimization procedure adopts the Newton–Raphson method as follows:

$$\left[\frac{\partial \mathbf{R}(\mathbf{U})}{\partial \mathbf{U}} \right]_{(n)} \{\Delta \mathbf{U}\} = -\{\mathbf{R}(\mathbf{U})\}_{(n)} \quad (34)$$

$$\mathbf{U}_{(n+1)} = \mathbf{U}_{(n)} + \alpha \cdot \Delta \mathbf{U} \quad (35)$$

The residual force (internal force) \mathbf{F}^{int} of the plastic work in Equation (33) can be obtained from the derivation of Equation (29) instead of Equation (25).

$$\begin{aligned} \mathbf{F}^{\text{(int)}} &= \int_{\Omega_e} \Delta \boldsymbol{\varepsilon}^T \hat{\mathbf{D}} \frac{\partial \Delta \mathbf{e}}{\partial \mathbf{U}} 2\pi r J \, d\xi \\ &= \int_{\Omega_e} \Delta \boldsymbol{\varepsilon}^T \hat{\mathbf{D}}^{(m)} \frac{\partial \Delta \boldsymbol{\varepsilon}}{\partial \mathbf{U}} 2\pi r J \, d\xi + \int_{\Omega_e} \Delta \boldsymbol{\varepsilon}^T \hat{\mathbf{D}}^{(mb)} \frac{\partial \Delta \boldsymbol{\kappa}}{\partial \mathbf{U}} 2\pi r J \, d\xi \\ &\quad + \int_{\Omega_e} \Delta \boldsymbol{\kappa}^T \hat{\mathbf{D}}^{(mb)} \frac{\partial \Delta \boldsymbol{\varepsilon}}{\partial \mathbf{U}} 2\pi r J \, d\xi + \int_{\Omega_e} \Delta \boldsymbol{\kappa}^T \hat{\mathbf{D}}^{(b)} \frac{\partial \Delta \boldsymbol{\kappa}}{\partial \mathbf{U}} 2\pi r J \, d\xi + \int_{\Omega_e} \Delta \boldsymbol{\gamma}^T \hat{\mathbf{D}}^{(s)} \frac{\partial \Delta \boldsymbol{\gamma}}{\partial \mathbf{U}} 2\pi r J \, d\xi \end{aligned} \quad (36)$$

Furthermore, the stiffness matrix in Equation (34) of the plastic work is derived by differentiating Equation (36) as follows:

$$\begin{aligned} \mathbf{K}^{(e)} &= \int_{\Omega_e} \frac{\partial \Delta \boldsymbol{\varepsilon}^T}{\partial \mathbf{U}} \hat{\mathbf{D}}^{(m)} \frac{\partial \Delta \boldsymbol{\varepsilon}}{\partial \mathbf{U}} 2\pi r J \, d\xi + \int_{\Omega_e} \frac{\partial \Delta \boldsymbol{\varepsilon}^T}{\partial \mathbf{U}} \hat{\mathbf{D}}^{(mb)} \frac{\partial \Delta \boldsymbol{\kappa}}{\partial \mathbf{U}} 2\pi r J \, d\xi \\ &\quad + \int_{\Omega_e} \frac{\partial \Delta \boldsymbol{\kappa}^T}{\partial \mathbf{U}} \hat{\mathbf{D}}^{(mb)} \frac{\partial \Delta \boldsymbol{\varepsilon}}{\partial \mathbf{U}} 2\pi r J \, d\xi + \int_{\Omega_e} \frac{\partial \Delta \boldsymbol{\kappa}^T}{\partial \mathbf{U}} \hat{\mathbf{D}}^{(b)} \frac{\partial \Delta \boldsymbol{\kappa}}{\partial \mathbf{U}} 2\pi r J \, d\xi \\ &\quad + \int_{\Omega_e} \Delta \boldsymbol{\varepsilon}^T \hat{\mathbf{D}}^{(m)} \frac{\partial^2 \Delta \boldsymbol{\varepsilon}}{\partial \mathbf{U} \partial \mathbf{U}} 2\pi r J \, d\xi + \int_{\Omega_e} \Delta \boldsymbol{\varepsilon}^T \hat{\mathbf{D}}^{(mb)} \frac{\partial^2 \Delta \boldsymbol{\kappa}}{\partial \mathbf{U} \partial \mathbf{U}} 2\pi r J \, d\xi \\ &\quad + \int_{\Omega_e} \Delta \boldsymbol{\kappa}^T \hat{\mathbf{D}}^{(mb)} \frac{\partial^2 \Delta \boldsymbol{\varepsilon}}{\partial \mathbf{U} \partial \mathbf{U}} 2\pi r J \, d\xi + \int_{\Omega_e} \Delta \boldsymbol{\kappa}^T \hat{\mathbf{D}}^{(b)} \frac{\partial^2 \Delta \boldsymbol{\kappa}}{\partial \mathbf{U} \partial \mathbf{U}} 2\pi r J \, d\xi \\ &\quad + \int_{\Omega_e} \frac{\partial \Delta \boldsymbol{\gamma}^T}{\partial \mathbf{U}} \hat{\mathbf{D}}^{(s)} \frac{\partial \Delta \boldsymbol{\gamma}}{\partial \mathbf{U}} 2\pi r J \, d\xi + \int_{\Omega_e} \Delta \boldsymbol{\gamma}^T \hat{\mathbf{D}}^{(s)} \frac{\partial^2 \Delta \boldsymbol{\gamma}}{\partial \mathbf{U} \partial \mathbf{U}} 2\pi r J \, d\xi \\ &\quad + \int_{\Omega_e} \left(\frac{\partial \Delta \boldsymbol{\varepsilon}^T}{\partial \mathbf{U}} \hat{\mathbf{H}}^{(m1)} + \frac{\partial \Delta \boldsymbol{\kappa}^T}{\partial \mathbf{U}} \hat{\mathbf{H}}^{(m2)} \right) \frac{\partial \Delta \boldsymbol{\varepsilon}}{\partial \mathbf{U}} 2\pi r J \, d\xi \\ &\quad + \int_{\Omega_e} \left(\frac{\partial \Delta \boldsymbol{\varepsilon}^T}{\partial \mathbf{U}} \hat{\mathbf{H}}^{(mb1)} + \frac{\partial \Delta \boldsymbol{\kappa}^T}{\partial \mathbf{U}} \hat{\mathbf{H}}^{(mb2)} \right) \frac{\partial \Delta \boldsymbol{\kappa}}{\partial \mathbf{U}} 2\pi r J \, d\xi \end{aligned}$$

$$\begin{aligned}
 & + \int_{\Omega_e} \left(\frac{\partial \Delta \varepsilon^T}{\partial \mathbf{U}} \hat{\mathbf{H}}^{(mb1)} + \frac{\partial \Delta \kappa^T}{\partial \mathbf{U}} \hat{\mathbf{H}}^{(mb2)} \right) \frac{\partial \Delta \varepsilon}{\partial \mathbf{U}} 2\pi r J \, d\xi \\
 & + \int_{\Omega_e} \left(\frac{\partial \Delta \varepsilon^T}{\partial \mathbf{U}} \hat{\mathbf{H}}^{(b1)} + \frac{\partial \Delta \kappa^T}{\partial \mathbf{U}} \hat{\mathbf{H}}^{(b2)} \right) \frac{\partial \Delta \kappa}{\partial \mathbf{U}} 2\pi r J \, d\xi \tag{37}
 \end{aligned}$$

The matrices $\hat{\mathbf{H}}^{(m1)}$, $\hat{\mathbf{H}}^{(m2)}$, $\hat{\mathbf{H}}^{(mb1)}$, $\hat{\mathbf{H}}^{(mb2)}$ and $\hat{\mathbf{H}}^{(b1)}$, $\hat{\mathbf{H}}^{(b2)}$, which come from the differentiation of the matrices $\hat{\mathbf{D}}^{(m)}$, $\hat{\mathbf{D}}^{(mb)}$ and $\hat{\mathbf{D}}^{(b)}$, are derived in Appendix B. The matrices $\hat{\mathbf{H}}$ are also integrated through the thickness direction as the matrices $\hat{\mathbf{D}}$.

Unlike the above formulae of the shell element, the inverse analysis using membrane elements does not perform integration through the thickness direction. The residual force and the stiffness matrix of inverse analysis with membrane elements have very simple forms and can be written as

$$\mathbf{F}^{(int)} = \int_{\Omega_e} \Delta \varepsilon^T \mathbf{D}^{(m)} \frac{\partial \Delta \varepsilon}{\partial S} 2\pi r J \, d\xi \tag{38}$$

$$\begin{aligned}
 \mathbf{K}^{(e)} & = \int_{\Omega_e} \frac{\partial \Delta \varepsilon^T}{\partial S} \mathbf{D}^{(m)} \frac{\partial \Delta \varepsilon}{\partial S} 2\pi r J \, d\xi + \int_{\Omega_e} \Delta \varepsilon^T \mathbf{D}^{(m)} \frac{\partial^2 \Delta \varepsilon}{\partial S \partial S} 2\pi r J \, d\xi \\
 & + \int_{\Omega_e} \Delta \varepsilon^T \frac{\partial \Delta \mathbf{D}^{(m)}}{\partial S} \frac{\partial \Delta \varepsilon}{\partial S} 2\pi r J \, d\xi \tag{39}
 \end{aligned}$$

A three-node quadratic element is used for the axisymmetric shell and membrane formulation of finite element inverse analysis. The integration in the thickness direction of the matrices $\hat{\mathbf{D}}$ and $\hat{\mathbf{H}}$ are performed using five point Simpson’s rule [42, 43].

5. NUMERICAL PROCEDURE FOR MULTI-STEP INVERSE ANALYSIS

The numerical procedure for multi-step inverse analysis is quite different from the conventional incremental analysis. In this section, the fundamental procedures and requirements of a multi-step inverse analysis are illustrated.

First, inverse analysis requires a desired final geometry (mid-surface) as the input data. This desired final shape is then constructed by finite element mesh. In this paper, three-node quadratic membrane and shell elements are used. The material properties for the initial blank should also be provided before solving the problem.

Secondly, it is necessary to assume the tooling and process conditions such as punch and die geometries, punch stroke, binder force, and friction, etc. These kinds of tooling conditions are usually determined by either knowledge-based criterion or they can be modified through an optimization algorithm outside this inverse analysis loop. Based on the tooling conditions and the desired final shape, sliding curves can be established. The purpose of sliding curves is to guide the movement of nodal points during the Newton–Raphson iterations so that nodal points can exist only on the sliding curves. Figure 2 is the schematic description of sliding curves of step n in the analysis of a conical cup drawing. The sliding curves of Zones I and V shown in Figure 2 are assumed using the flat surfaces of the punch and the die. Those of Zones II and IV are assumed on the corner arcs of the punch and die. For Zone III, which is assumed as the straight line,

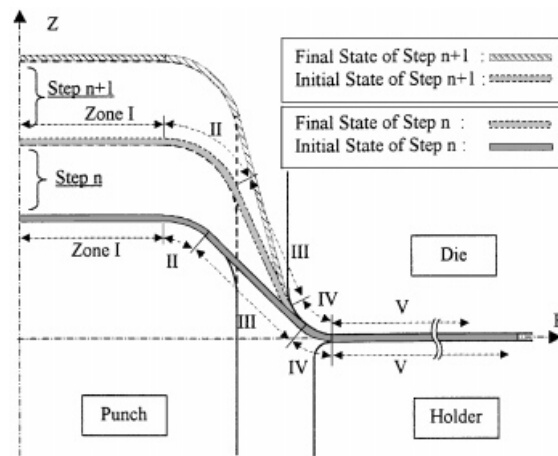


Figure 2. Assumption of sliding curves for multi-step inverse analysis.

the sliding surface lies on the tangent line between the two arcs of the punch and die. Two end points of Zone III can easily be obtained from a simple geometric calculation. During a real deep drawing process, material may not fall on the sliding curves. However, the differences between positions of material and sliding curves are quite small in many drawing processes.

Thirdly, nodal points should be initialized on the sliding curves for the initial blank and intermediate shapes using the desired final mesh geometry. A simple method for the initialization can be found in Majlessi and Lee's paper [29]. Their approach is summarized as follows:

$$\begin{aligned}
 &\text{do } n = \text{final step, first step, } -1 \\
 &\quad S_1^n = s_1^n \\
 &\quad S_i^n = S_{i-1}^n + \delta \cdot (s_i^n - s_{i-1}^n), \quad i = 2, 3, \dots, m \\
 &\text{enddo}
 \end{aligned}
 \tag{40}$$

S_i^n, s_i^n are the positions of nodal point i along the meridian curves at the initial and final states of step n , respectively. δ is an arbitrary number less than unity, and m denotes the total number of nodal points. The initialization procedure is important because the convergence of the global and Newton–Raphson iterations sometimes depends on the initialization. This means Newton–Raphson iterations could diverge when the initialization is far from the desirable solution.

Finally, the multi-step inverse analysis is performed according to the flow chart in Figure 3. The global iterations are carried out in the same manner as Majlessi and Lee's procedure. Newton–Raphson iterations for all steps are performed inside the global iterations. Two configurations of step n and step $n+1$ are shown in Figure 2 to explain Newton–Raphson iterations. Newton–Raphson iterations of step n consider the initial state and the final state of step n . After the convergence of Newton–Raphson iterations of step n , the state variables, such as plastic strains, thickness at integration points and the rotation ω at nodes, are updated for the final state of step n . However, the nodal positions \mathbf{X} of the initial state of step n , not of the final state, are updated. And then, the final state of step n becomes the initial state of step $n+1$ during the next Newton–Raphson iterations of step $n+1$ as shown in Figure 2.

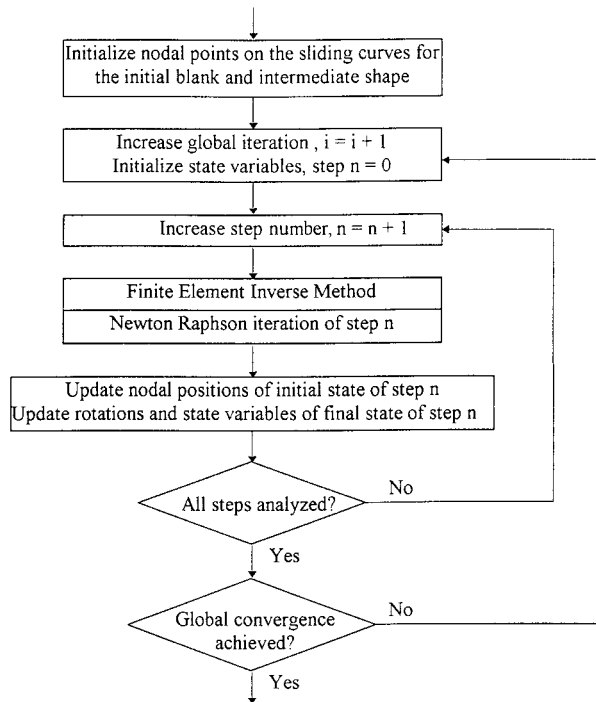


Figure 3. Flow chart of the multi-step inverse analysis.

Newton–Raphson iterations for each step are performed until two convergence criteria for the displacement and the residual force shown in Equation (41) are satisfied simultaneously.

$$\left\| \frac{\Delta \mathbf{U}}{\mathbf{U}} \right\|_2 \leq \varepsilon_D, \quad \|\mathbf{R}\|_2 \leq \varepsilon_F \quad (41)$$

where $\|\cdot\|_2$ means the Euclidean norm. Tolerances ε_D and ε_F are small values, which have the order of 10^{-5} and 10^{-2} , respectively, in this paper. The convergence criterion for the global iterations is

$$\frac{\sum_{n=1}^{\text{Final step}} \|\mathbf{U}\|_2}{\text{Total number of steps}} \leq \varepsilon_{GD} \quad (42)$$

where the value of ε_{GD} used in this paper is between 10^{-2} and 10^{-1} .

6. NUMERICAL EXAMPLES

The present algorithm described above has been implemented in a finite element code and applied to two deep drawing problems. One is a drawing of a thin sheet and the other of a relatively thicker sheet material. We considered the incremental analysis as virtual experiments for checking the validity and accuracy of the present algorithm. The final deformed shape of the mid-surface,

which is the input data of the inverse analysis, was obtained from the incremental analyses[‡] (ABAQUS analysis with shell and solid elements). Thus, inverse analysis (IA) calculates the initial blank size, intermediate shapes and strain distributions. These results are compared with those of the incremental analyses, in which the initial blank size is given.

6.1. Example 1: Deep drawing of a thin sheet metal

The setup of this deep drawing problem is taken from the ABAQUS Examples manual [44]. The material properties and the process variables are shown below for the inverse and ABAQUS analysis.

Stress–strain curve	$\bar{\sigma} = 513\bar{\epsilon}^{0.223}$ MPa
Lankford value	$r = 1.0$
Initial sheet thickness	$t_0 = 0.82$ mm
Initial blank diameter	$\Phi_B = 200$ mm for ABAQUS analysis.
Friction coefficient	$\mu = 0.25$ at punch and 0.1 at die and blank holder.
Blank holding force	$F_B = 100$ kN

The Young's modulus is 211 GPa and the Poisson's ratio is 0.3. The tooling geometry is shown in Figure 4. The punch stroke of this example is 60 mm. ABAQUS solved this deep drawing problem using 100 quadratic axisymmetric shell elements to determine the final deformed shape, strain distribution, etc. ABAQUS analysis was performed with 542 incremental steps for the frictional case. The flange diameter of the drawn cup after ABAQUS analysis is 135.82 mm for the above frictional condition, and 133.7 mm for no frictional condition. Using the final deformed shape obtained from ABAQUS analysis and the above process conditions, multi-step inverse analyses have been performed using 100 quadratic membrane and shell elements, respectively. The initial blank diameter, intermediate shapes and strain distribution were obtained after the inverse analyses. Figure 5 displays the result of the 6-step inverse analysis. To solve the 6-step problem, the inverse analysis took seven global iterations and an average of 31 Newton–Raphson iterations within each global iteration. Note that the initial blank and intermediate shapes were assumed by the initial guess scheme and then were calculated by the inverse analysis as shown in Figure 5. Since the total stroke is 60 mm, a 10 mm punch increment is assumed for each analysis step of the 6-step inverse analysis. Therefore, the punch increment per step is much larger than that in the conventional incremental analysis.

Table I shows the predicted initial blank diameters obtained from the inverse analysis with various combinations of element type, step size, and frictional condition. All of the predicted blank sizes have less than 2 per cent error compared with the original blank size. For this reason, if the blank size is the only required design parameter, 1-step analysis using the membrane element, which is fast and simple, may give a good solution for the thin sheet metal forming process. Note that the oscillation of blank size in the frictional case comes partially from the simplified frictional boundary condition and partly from the termination criterion of the global iteration. However, the range of error is less than 0.75 per cent, which is insignificant.

[‡] Notice in the remaining of this paper, ABAQUS analysis is referred to the incremental forward finite element method using a commercial software package ABAQUS/Standard.

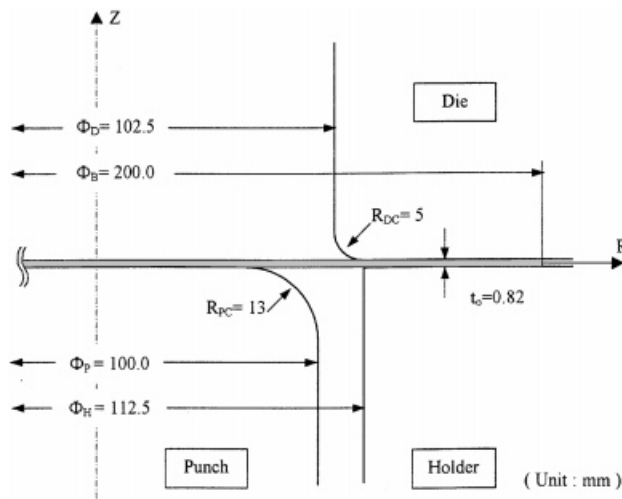


Figure 4. Tooling geometry for the deep drawing problem.

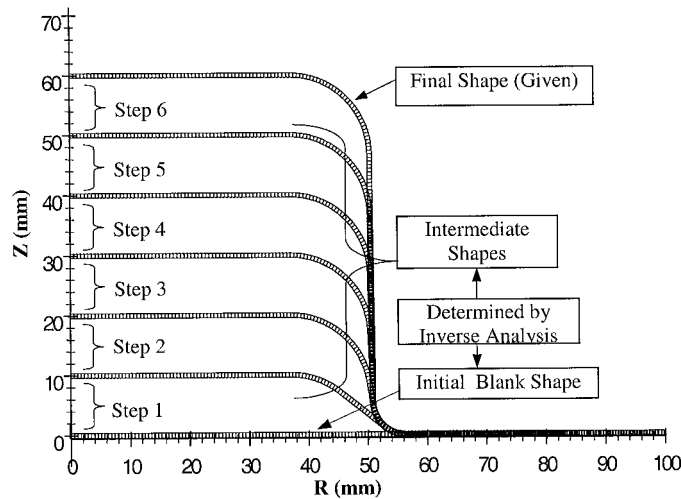


Figure 5. Six-step inverse analysis using shell elements.

Notice that the strain distribution varies with the element type and analysis step size as shown in Figure 6. The radial and hoop strain distributions of 12-step inverse analysis with shell elements (IA-shell) are in better agreements with ABAQUS-shell results than those of 12-step inverse analysis with membrane elements (IA-membrane). Increasing the number of analysis steps hardly increased the accuracy of IA-membrane, whereas, Figure 7 demonstrates that the accuracy was

Table I. Predicted initial blank diameters for Example 1 from various inverse analyses. (Unit: mm).

IA type		1-Step IA	3-Step IA	6-Step IA	12-Step IA
Punch move per step		60.00	20.00	10.00	5.00
No friction	Membrane	202.14	202.68	203.00	203.02
	Shell	202.04	202.24	201.88	201.14
Friction	Membrane	199.52	199.36	199.54	199.58
	Shell	199.96	200.06	199.65	198.52

Original blank diameter in ABAQUS analysis = 200 mm (friction and no friction)

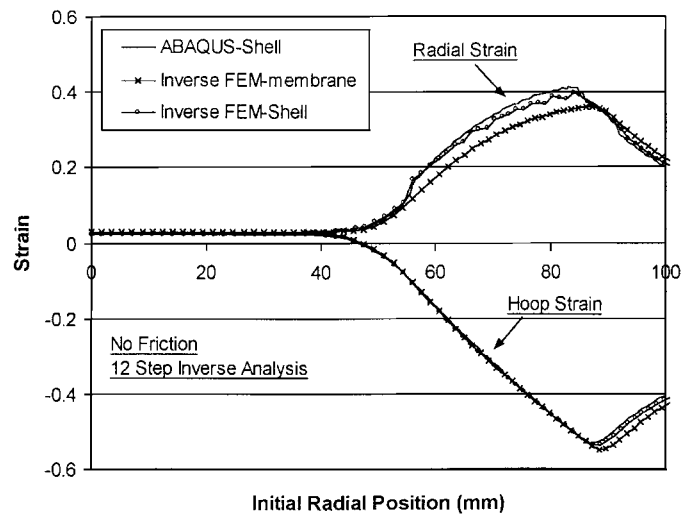


Figure 6. Comparison of strain distribution of mid-surface between the incremental FEM, IA with shell formulation and IA with membrane formulation: no friction.

improved by using multi-step IA-shell. In order to consider the bending effect and to improve the prediction accuracy of strain distribution, Figure 7 shows that multi-step analysis with shell elements is required in inverse analysis. The fluctuations of the radial strain curves shown in Figure 7 come from the relatively large punch displacement per increment. For example, 6-step IA has a 10 mm punch displacement per increment. Therefore, the material jumps into and out of the bending and unbending region in an abrupt manner. The strain distributions of IA-shell for the top and bottom surfaces agree with the ABAQUS results very well as shown in Figure 8, with only a small discrepancy in the region of the cup wall. Figure 9 compares the strain distributions between two IA solutions and the ABAQUS results for the frictional condition. The analysis with IA-membrane provides large strain values at the centre region of the cup, because it does not have bending resistance at the punch shoulder. This tendency of over-predicting the strain at the centre region is usually found when membrane elements are used even in the incremental analysis. However, the values of IA-shell in this region are similar to those of ABAQUS-shell, even though the results of IA-shell are calculated using only six steps.

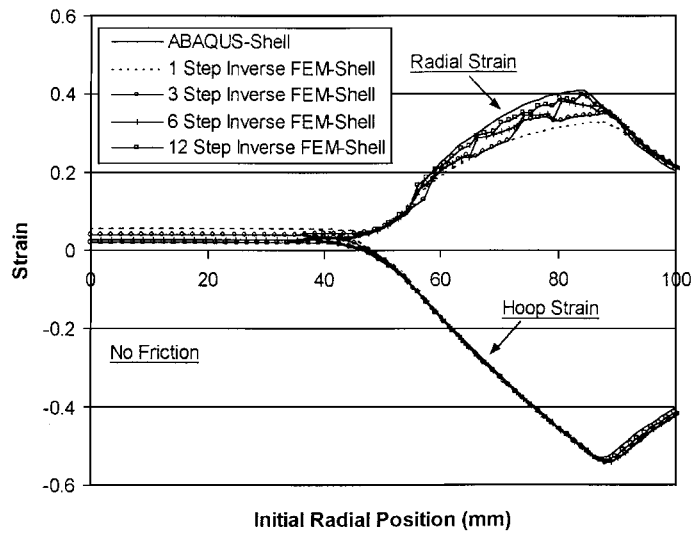


Figure 7. Variation of strain distribution of mid-surface according to the increment of analysis step for IA with shell formulation: no friction.

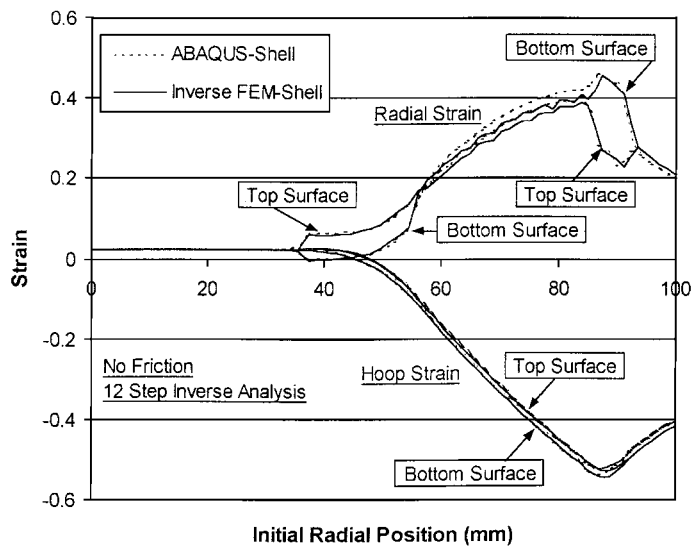


Figure 8. Strain distribution of top and bottom surfaces for the incremental FEM and IA with shell formulation: no friction.

The CPU time of the analyses on a HP C180 workstation are listed in Table II. The CPU time increases as an increase of analysis step for both IA-membrane and IA-shell. IA-shell takes much more CPU time compared to IA-membrane. However, the accuracy of IA-shell is generally better than that of IA-membrane and the CPU time of IA-shell is much shorter than that of conventional increment analysis (Table II).

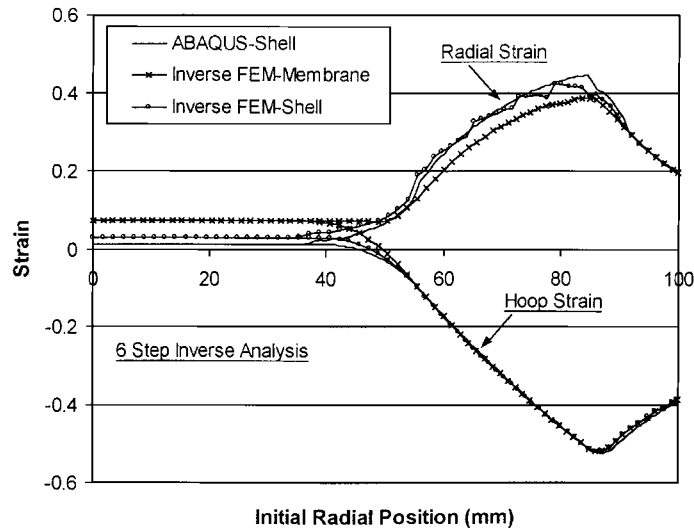


Figure 9. Comparison of strain distribution of mid-surface between the incremental FEM, IA with shell formulation and IA with membrane formulation for frictional condition.

6.2. Example 2: Deep drawing of a relatively thick sheet metal

The thickness of the initial blank in this example differs greatly from that of the first example. The sheet thickness is changed from 0.82 to 4.0 mm. To compensate for the increased thickness, the die diameter (Φ_D) is increased from 102.5 to 111.0 mm and the corresponding blank hold diameter (Φ_H) is changed from 112.5 to 121.0 mm. However, the corner radii of the punch (R_{PC}) and the die (R_{DC}) remain the same. The material in this example undergoes a severe bending and unbending process because the ratio of the sheet thickness over the corner radius of the die (t_0/R_{DC}) is increased from 0.82/5 to 4.0/5. Finally, the blank diameter is reduced to 180 mm, the punch stroke is changed to 50 mm, and the blank holding force is increased to 400 kN for a successful forming. All the other material properties and process conditions are the same as those in the first example. ABAQUS analysis was performed by 8-node solid elements with reduced integration. The finite element model for ABAQUS analysis has four layers through the thickness direction, and 100 elements along the radial direction. The inverse analyses for this example use 100 quadratic shell and membrane elements. ABAQUS analysis performed with 172 incremental steps, while the number of the global iterations was 6 and the typical number of the Newton–Raphson iterations was 40 in the 5-step inverse analysis.

In Table III, the predicted initial blank diameters by IA-membrane and IA-shell are compared with the initial input in the forward analysis. Errors of both IA-membrane and IA-shell are increased as the sheet thickness is increased. The blank diameters of IA-membrane have about 5 per cent error regardless of the analysis step number. However, the blank diameters of IA-shell range from having 4 to 1 per cent error. Table III shows that the IA-shell can reduce the error sufficiently by increasing the analysis step.

The strain distributions with respect to the mid-surface at the initial state are compared among IA-membrane, IA-shell and ABAQUS-Solid in Figure 10. Both the hoop and radial strains of

Table II. CPU time of inverse analyses for Example 1 according to various cases. (Unit: s)

IA type		1-Step IA	3-Step IA	6-Step IA	12-Step IA
No friction	Membrane	0.6	6.0	20.0	70.1
	Shell	2.0	33.2	118.5	351.5
Friction	Membrane	0.9	11.0	31.8	115.8
	Shell	2.9	38.5	130.6	469.2

ABAQUS-Shell = 2889.9 s (no friction), 3228.0 s (friction)

Table III. Predicted initial blank diameters for Example 2 from various inverse analyses. (Unit: mm).

IA type	1-Step IA	2-Step IA	5-Step IA	10-Step IA
Punch move per step	50.00	25.00	10.00	5.00
Membrane	189.42	189.94	190.14	190.08
Shell	187.86	186.50	183.10	182.00

Original blank diameter in ABAQUS analysis = 180 mm (with friction)

IA-membrane have quite large errors, especially in the region of the bending and unbending. IA-shell also has some error in that region. But the tendency of IA-shell curve is similar to those of ABAQUS-Solid. As expected, the error of IA-shell is relatively quite small than that of IA-membrane when the initial blank is a relatively thick sheet and the deformation undergoes a severe bending and unbending process. Because of the basic assumption of shell element, the initial mid-surface of shell element differs from that of solid element at the final state especially for the thick sheet case. Therefore, the difference of strain between an incremental analysis with shell element (ABAQUS-Shell) and an incremental analysis with solid element (ABAQUS-Solid) may be similar to that of strain between IA-shell and ABAQUS-Solid. Because the initial mid-surfaces of solid and shell elements become different surfaces at the final state, the strain distributions of top and bottom surfaces are compared in Figure 11. Except for the radial strains of top surface from 60 to 75 mm region, the strain distributions of IA-shell closely follow those of ABAQUS-Solid.

The better predictions of the initial blank size and the strain distribution in multi-step inverse analysis compared to those of the one-step formulation are due to its ability to capture non-linear strain paths in the forming process. Figure 12 illustrates the strain paths of one material point near the die radius obtained from the forward FEM analysis (the solid line), the multi-step inverse analysis (the dash-dotted line) and the one-step inverse analysis (the dashed line). Notice that the first two methods provide very similar strain paths, while the one-step inverse analysis has a large discrepancy.

The CPU time on a HP C180 workstation for multi-step IA-membrane, multi-step IA-shell, and ABAQUS-Solid are compared in Table IV. When considering both CPU time and accuracy, the above results show that multi-step IA-shell is more desirable for calculating design variables than multi-step IA-membrane or incremental analysis. In fact, the comparison of the inverse analysis with the direct analysis of ABAQUS is not appropriate, since they solved different problems. If the incremental FEM with sensitivity analysis is used to solve the same problem such as a blank

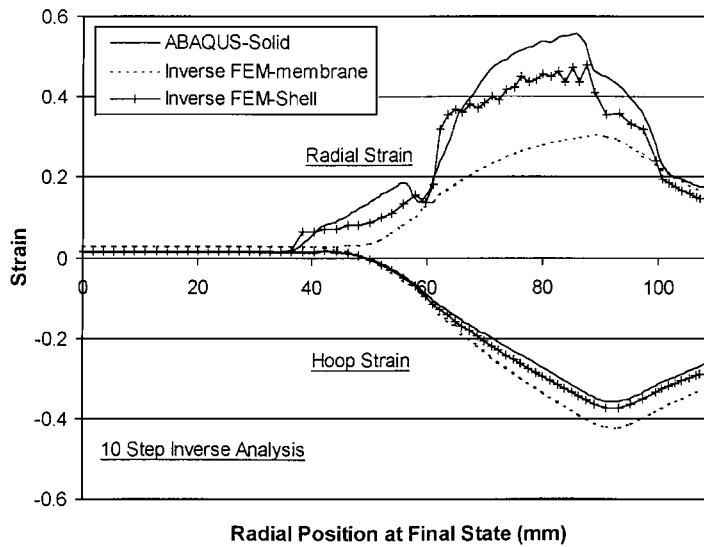


Figure 10. Comparison of strain distribution of mid-surface between the incremental FEM, IA with shell formulation and IA with membrane formulation for the case of thick blank.

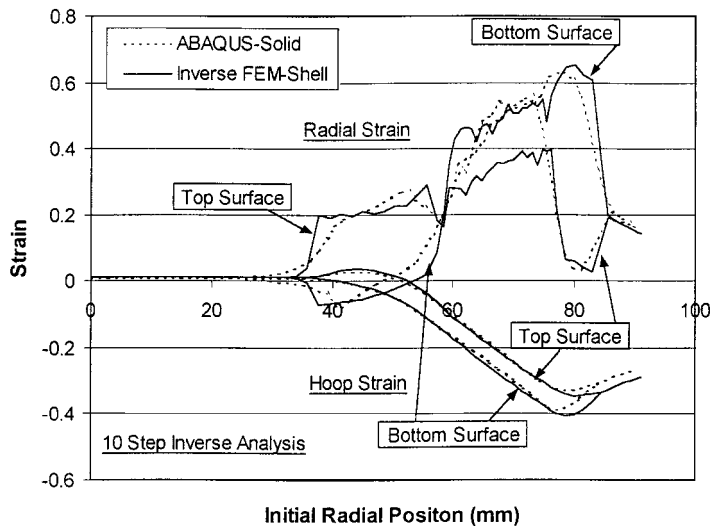


Figure 11. Strain distribution of top and bottom surfaces for the incremental FEM and IA with shell formulation.

design problem, the incremental FEM simulation needs to solve the forward process at least three times, and in many cases, from five to more than ten times. Thus, the advantage of the inverse analysis in the design process is obvious.

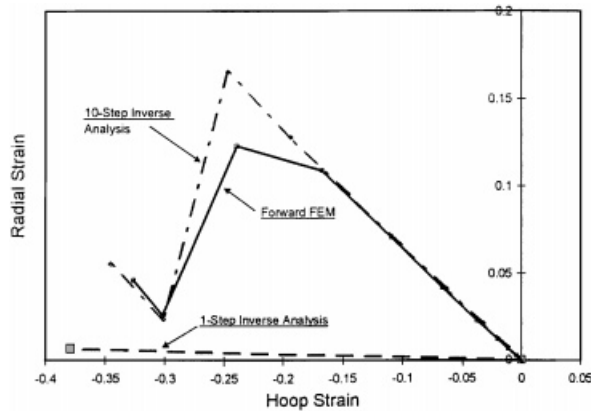


Figure 12. Strain paths of one material point near the die radius obtained from various simulation methods.

Table IV. CPU time of inverse analyses for Example 2 according to various cases. (Unit: s).

IA type	1-Step IA	2-Step IA	5-Step IA	10-Step IA
Membrane	0.9	7.8	27.3	80.9
Shell	2.9	19.5	116.8	401.2
ABAQUS-Solid = 1430.0 s				

7. CONCLUSIONS

Given the desired final configuration, inverse finite element analysis (IA) calculates the original configuration and the corresponding strain/stress distributions taking the material deformation behaviour into account. The method is particularly useful at the early design stage where rapid assessment of formability is required. In the past, most of the inverse analyses have utilized membrane elements and one-step formulation to achieve the desired calculation speed. However, the solution is not accurate enough (Figure 10) when the deformation path is not that linear and when bending/unbending effect is not negligible, typically the cases in industrial applications. With the development of computer technology, more accurate formulation is desired. In this paper, an axisymmetric shell formulation of the multi-step inverse analysis has been developed to improve the accuracy of the calculated initial blank shape and the strain distribution in deep drawing processes. As the number of analysis steps is increased, this approach is more accurate in following more realistic deformation path (Figure 12) and boundary conditions. The developed IA-shell formulation considers the bending and unbending phenomena. The numerical results of thin and thick sheet deep drawing demonstrate that the present algorithm provides accurate prediction of the initial blank size and the strain distributions. Our algorithm will be further tested in designing the optimal tooling geometry of some axisymmetric parts in production.

APPENDIX A

The reaction force \mathbf{t} can be obtained from the derivation of the plastic work by \mathbf{x} at the final state using the concept of the force equilibrium. Then,

$$\begin{aligned} \mathbf{t} &= \int_{\Omega_e} \Delta \mathbf{e}^T \hat{\mathbf{D}} \frac{\partial \Delta \mathbf{e}}{\partial \mathbf{x}} 2\pi r J \, d\xi \\ &= \int_{\Omega_e} \Delta \varepsilon^T \hat{\mathbf{D}}^{(m)} \frac{\partial \Delta \varepsilon}{\partial \mathbf{x}} 2\pi r J \, d\xi + \int_{\Omega_e} \Delta \varepsilon^T \hat{\mathbf{D}}^{(mb)} \frac{\partial \Delta \kappa}{\partial \mathbf{x}} 2\pi r J \, d\xi \\ &\quad + \int_{\Omega_e} \Delta \kappa^T \hat{\mathbf{D}}^{(mb)} \frac{\partial \Delta \varepsilon}{\partial \mathbf{x}} 2\pi r J \, d\xi + \int_{\Omega_e} \Delta \kappa^T \hat{\mathbf{D}}^{(b)} \frac{\partial \Delta \kappa}{\partial \mathbf{x}} 2\pi r J \, d\xi \end{aligned} \quad (\text{A1})$$

The above strain derivatives are expressed in the following:

$$\delta \varepsilon_{11}^f = \delta \ln(\Delta \lambda_1) = \frac{1}{\Delta \lambda_1^2 G_{11}} \frac{d\mathbf{x}}{d\xi} \cdot \frac{d\delta \mathbf{x}}{d\xi} \quad (\text{A2})$$

$$\delta \varepsilon_{22}^f = \delta \ln(\Delta \lambda_2) = \frac{1}{\Delta \lambda_2} \frac{\delta r}{R} \quad (\text{A3})$$

$$\begin{aligned} \delta \tilde{\kappa}_{11}^f &= \delta \left[\frac{\lambda_t^0}{g_{11} \Delta \lambda_1 \Delta \lambda_2} (b_{11} - \Delta \lambda_1 B_{11}) \right] \\ &= \frac{\lambda_t^0}{g_{11} \Delta \lambda_1 \Delta \lambda_2} \left\{ \frac{1}{\Delta \lambda_1^2 G_{11}} (-3b_{11} + 2\Delta \lambda_1 B_{11}) \frac{d\mathbf{x}}{d\xi} \cdot \frac{d\delta \mathbf{x}}{d\xi} - (b_{11} - \Delta \lambda_1 B_{11}) \frac{\delta r}{r} \right. \\ &\quad \left. + \frac{d\mathbf{n}}{d\xi} \cdot \frac{d\delta \mathbf{x}}{d\xi} + \mathbf{t} \cdot \frac{d\mathbf{x}}{d\xi} \frac{d\delta \omega}{d\xi} + \frac{d\mathbf{t}}{d\xi} \cdot \frac{d\mathbf{x}}{d\xi} \delta \omega \right\} \end{aligned} \quad (\text{A4})$$

$$\begin{aligned} \delta \tilde{\kappa}_{22}^f &= \delta \left[\frac{\lambda_t^0}{g_{22} \Delta \lambda_1 \Delta \lambda_2} (b_{22} - \Delta \lambda_2 B_{22}) \right] \\ &= \frac{\lambda_t^0}{g_{22} \Delta \lambda_1 \Delta \lambda_2} \left\{ \frac{1}{\Delta \lambda_1^2 G_{11}} (-b_{22} + \Delta \lambda_2 B_{22}) \frac{d\mathbf{x}}{d\xi} \cdot \frac{d\delta \mathbf{x}}{d\xi} \right. \\ &\quad \left. + \frac{1}{R} \left(-\frac{3b_{22}}{\Delta \lambda_2} + 2B_{22} \right) \delta r + n_r \delta r - n_z r \delta \omega \right\} \end{aligned} \quad (\text{A5})$$

The superscript ‘f’ in Equations (A2)–(A4) means that the variation of the strain components is derived according to the variation of \mathbf{x} and ω at time $t = t_0 + \Delta t$.

APPENDIX B

When we construct the stiffness matrix by the differentiation of the residual force in Equation (37), the matrices $\hat{\mathbf{D}}$ should be differentiated by \mathbf{U} . Then the stiffness including the matrices

$\partial \hat{\mathbf{D}}^{(m)}/\partial \mathbf{U}, \partial \hat{\mathbf{D}}^{(mb)}/\partial \mathbf{U}, \partial \hat{\mathbf{D}}^{(b)}/\partial \mathbf{U}$ and $\partial \hat{\mathbf{D}}^{(s)}/\partial \mathbf{U}$ can be written as

$$\begin{aligned} \mathbf{K}^{(e)} = & \text{The first 10 terms in Equation (38)} \\ & + \int_{\Omega_e} \Delta \varepsilon^T \frac{\partial \hat{\mathbf{D}}^{(m)}}{\partial \mathbf{U}} \frac{\partial \Delta \varepsilon}{\partial \mathbf{U}} 2\pi r J \, d\xi + \int_{\Omega_e} \Delta \varepsilon^T \frac{\partial \hat{\mathbf{D}}^{(mb)}}{\partial \mathbf{U}} \frac{\partial \Delta \kappa}{\partial \mathbf{U}} 2\pi r J \, d\xi \\ & + \int_{\Omega_e} \Delta \kappa^T \frac{\partial \hat{\mathbf{D}}^{(mb)}}{\partial \mathbf{U}} \frac{\partial \Delta \varepsilon}{\partial \mathbf{U}} 2\pi r J \, d\xi + \int_{\Omega_e} \Delta \kappa^T \frac{\partial \hat{\mathbf{D}}^{(b)}}{\partial \mathbf{U}} \frac{\partial \Delta \kappa}{\partial \mathbf{U}} 2\pi r J \, d\xi \\ & + \int_{\Omega_e} \Delta \gamma^T \frac{\partial \hat{\mathbf{D}}^{(s)}}{\partial \mathbf{U}} \frac{\partial \Delta \gamma}{\partial \mathbf{U}} 2\pi r J \, d\xi \end{aligned} \tag{B1}$$

Then, the terms $\Delta \varepsilon^T \partial \hat{\mathbf{D}}^{(m)}/\partial \mathbf{U}, \Delta \varepsilon^T \partial \hat{\mathbf{D}}^{(mb)}/\partial \mathbf{U}, \Delta \kappa^T \partial \hat{\mathbf{D}}^{(mb)}/\partial \mathbf{U}, \Delta \kappa^T \partial \hat{\mathbf{D}}^{(b)}/\partial \mathbf{U}$ and $\Delta \gamma^T \partial \hat{\mathbf{D}}^{(s)}/\partial \mathbf{U}$ in the last five terms of Equation (B1) can be derived further as follows:

$$\begin{aligned} \Delta \varepsilon^T \frac{\partial \hat{\mathbf{D}}^{(m)}}{\partial \mathbf{U}} &= \Delta \varepsilon^T \frac{\partial}{\partial \mathbf{U}} \left(\int_{-0.5}^{0.5} \mathbf{D}^{(m)} J_t \, d\eta \right) = \Delta \varepsilon^T \frac{\partial}{\partial \mathbf{U}} \left(\int_{-0.5}^{0.5} c \frac{\bar{\sigma}}{\Delta \bar{\varepsilon}} \begin{bmatrix} 1 & b \\ b & 1 \end{bmatrix} J_t \, d\eta \right) \\ &= \Delta \varepsilon^T \int_{-0.5}^{0.5} c \frac{\partial}{\partial \Delta \bar{\varepsilon}} \left(\frac{\bar{\sigma}}{\Delta \bar{\varepsilon}} \right) \frac{\partial \Delta \bar{\varepsilon}}{\partial \Delta \varepsilon_{\alpha\alpha}^1} \frac{\partial \Delta \varepsilon_{\alpha\alpha}^1}{\partial \mathbf{U}} \begin{bmatrix} 1 & b \\ b & 1 \end{bmatrix} J_t \, d\eta \\ &= \int_{-0.5}^{0.5} c \frac{\partial}{\partial \Delta \bar{\varepsilon}} \left(\frac{\bar{\sigma}}{\Delta \bar{\varepsilon}} \right) \frac{\partial \Delta \bar{\varepsilon}}{\partial \Delta \varepsilon_{\alpha\alpha}^1} \left(\frac{\partial \Delta \varepsilon_{\alpha\alpha}}{\partial \mathbf{U}} + \eta \frac{\partial \Delta \kappa_{\alpha\alpha}}{\partial \mathbf{U}} \right) \begin{bmatrix} 1 & b \\ b & 1 \end{bmatrix} J_t \, d\eta \\ &= \frac{\partial \Delta \varepsilon_{\alpha\alpha}}{\partial \mathbf{U}} \Delta \varepsilon^T \int_{-0.5}^{0.5} c \frac{\partial}{\partial \Delta \bar{\varepsilon}} \left(\frac{\bar{\sigma}}{\Delta \bar{\varepsilon}} \right) \frac{\partial \Delta \bar{\varepsilon}}{\partial \Delta \varepsilon_{\alpha\alpha}^1} \begin{bmatrix} 1 & b \\ b & 1 \end{bmatrix} J_t \, d\eta \\ &\quad + \frac{\partial \Delta \kappa_{\alpha\alpha}}{\partial \mathbf{U}} \Delta \varepsilon^T \int_{-0.5}^{0.5} c \frac{\partial}{\partial \Delta \bar{\varepsilon}} \left(\frac{\bar{\sigma}}{\Delta \bar{\varepsilon}} \right) \frac{\partial \Delta \bar{\varepsilon}}{\partial \Delta \varepsilon_{\alpha\alpha}^1} \eta \begin{bmatrix} 1 & b \\ b & 1 \end{bmatrix} J_t \, d\eta \\ &= \frac{\partial \Delta \varepsilon}{\partial \mathbf{U}} \hat{\mathbf{H}}^{(m1)} + \frac{\partial \Delta \kappa}{\partial \mathbf{U}} \hat{\mathbf{H}}^{(m2)} \end{aligned} \tag{B2}$$

where

$$c = \frac{2(2+r)(1+r)}{3(1+2r)}, \quad b = \frac{r}{1+r}$$

and summed on $\alpha\alpha = 1, 2$ and also

$$\begin{aligned}
 \Delta \varepsilon^T \frac{\partial \hat{\mathbf{D}}^{(mb)}}{\partial \mathbf{U}} &= \Delta \varepsilon^T \frac{\partial}{\partial \mathbf{U}} \left(\int_{-0.5}^{0.5} \eta \mathbf{D}^{(m)} J_t \, d\eta \right) \\
 &= \frac{\partial \Delta \varepsilon_{\alpha\alpha}}{\partial \mathbf{U}} \Delta \varepsilon^T \int_{-0.5}^{0.5} c \frac{\partial}{\partial \Delta \bar{\varepsilon}} \left(\frac{\bar{\sigma}}{\Delta \bar{\varepsilon}} \right) \frac{\partial \Delta \bar{\varepsilon}}{\partial \Delta \varepsilon_{\alpha\alpha}^1} \eta \begin{bmatrix} 1 & b \\ b & 1 \end{bmatrix} J_t \, d\eta \\
 &\quad + \frac{\partial \Delta \kappa_{\alpha\alpha}}{\partial \mathbf{U}} \Delta \varepsilon^T \int_{-0.5}^{0.5} c \frac{\partial}{\partial \Delta \bar{\varepsilon}} \left(\frac{\bar{\sigma}}{\Delta \bar{\varepsilon}} \right) \frac{\partial \Delta \bar{\varepsilon}}{\partial \Delta \varepsilon_{\alpha\alpha}^1} \eta^2 \begin{bmatrix} 1 & b \\ b & 1 \end{bmatrix} J_t \, d\eta \\
 &= \frac{\partial \Delta \varepsilon}{\partial \mathbf{U}} \hat{\mathbf{H}}^{(mb1)} + \frac{\partial \Delta \kappa}{\partial \mathbf{U}} \hat{\mathbf{H}}^{(mb2)}
 \end{aligned} \tag{B3}$$

$$\begin{aligned}
 \Delta \kappa^T \frac{\partial \hat{\mathbf{D}}^{(mb)}}{\partial \mathbf{U}} &= \Delta \kappa^T \frac{\partial}{\partial \mathbf{U}} \left(\int_{-0.5}^{0.5} \eta \mathbf{D}^{(m)} J_t \, d\eta \right) \\
 &= \frac{\partial \Delta \varepsilon_{\alpha\alpha}}{\partial \mathbf{U}} \Delta \kappa^T \int_{-0.5}^{0.5} c \frac{\partial}{\partial \Delta \bar{\varepsilon}} \left(\frac{\bar{\sigma}}{\Delta \bar{\varepsilon}} \right) \frac{\partial \Delta \bar{\varepsilon}}{\partial \Delta \varepsilon_{\alpha\alpha}^1} \eta \begin{bmatrix} 1 & b \\ b & 1 \end{bmatrix} J_t \, d\eta \\
 &\quad + \frac{\partial \Delta \kappa_{\alpha\alpha}}{\partial \mathbf{U}} \Delta \kappa^T \int_{-0.5}^{0.5} c \frac{\partial}{\partial \Delta \bar{\varepsilon}} \left(\frac{\bar{\sigma}}{\Delta \bar{\varepsilon}} \right) \frac{\partial \Delta \bar{\varepsilon}}{\partial \Delta \varepsilon_{\alpha\alpha}^1} \eta^2 \begin{bmatrix} 1 & b \\ b & 1 \end{bmatrix} J_t \, d\eta \\
 &= \frac{\partial \Delta \varepsilon}{\partial \mathbf{U}} \hat{\mathbf{H}}^{(mb3)} + \frac{\partial \Delta \kappa}{\partial \mathbf{U}} \hat{\mathbf{H}}^{(mb4)}
 \end{aligned} \tag{B4}$$

$$\begin{aligned}
 \Delta \kappa^T \frac{\partial \hat{\mathbf{D}}^{(b)}}{\partial \mathbf{U}} &= \Delta \kappa^T \frac{\partial}{\partial \mathbf{U}} \left(\int_{-0.5}^{0.5} \eta^2 \mathbf{D}^{(m)} J_t \, d\eta \right) \\
 &= \frac{\partial \Delta \varepsilon_{\alpha\alpha}}{\partial \mathbf{U}} \Delta \kappa^T \int_{-0.5}^{0.5} c \frac{\partial}{\partial \Delta \bar{\varepsilon}} \left(\frac{\bar{\sigma}}{\Delta \bar{\varepsilon}} \right) \frac{\partial \Delta \bar{\varepsilon}}{\partial \Delta \varepsilon_{\alpha\alpha}^1} \eta^2 \begin{bmatrix} 1 & b \\ b & 1 \end{bmatrix} J_t \, d\eta \\
 &\quad + \frac{\partial \Delta \kappa_{\alpha\alpha}}{\partial \mathbf{U}} \Delta \kappa^T \int_{-0.5}^{0.5} c \frac{\partial}{\partial \Delta \bar{\varepsilon}} \left(\frac{\bar{\sigma}}{\Delta \bar{\varepsilon}} \right) \frac{\partial \Delta \bar{\varepsilon}}{\partial \Delta \varepsilon_{\alpha\alpha}^1} \eta^3 \begin{bmatrix} 1 & b \\ b & 1 \end{bmatrix} J_t \, d\eta \\
 &= \frac{\partial \Delta \varepsilon}{\partial \mathbf{U}} \hat{\mathbf{H}}^{(b1)} + \frac{\partial \Delta \kappa}{\partial \mathbf{U}} \hat{\mathbf{H}}^{(b2)}
 \end{aligned} \tag{B5}$$

Using Equations (B2)–(B5) and $\partial \hat{\mathbf{D}}^{(s)}/\partial \mathbf{U} = \mathbf{0}$, Equation (B1) becomes Equation (38).

ACKNOWLEDGEMENTS

This work was funded in part through a Ford gift, a NSF grant number DMI-9703249 to J. C. and a KOSEF (Korea Science & Engineering Foundation) post-doctoral fellowship to C. H. L.

REFERENCES

1. Badrinarayanan S, Zabarar N. A sensitivity analysis for the optimal design of metal forming processes. *Computer Methods in Applied Mechanics and Engineering* 1996; **129**:319–348.
2. Badrinarayanan S, Zabarar N. Preform design in metal forming. In *Proceedings of the International Conference on NUMIFORM'95*, Balkema, Ithaca, NY, Shen SF, Dawson PR (eds). 1995; 533–538.
3. Fourment L, Chenot JL. Optimal design for non-steady state metal forming process—I. Shape Optimization Method. *International Journal for Numerical Methods in Engineering* 1996; **39**:33–50.
4. Fourment L, Chenot JL. Optimal design for non-steady state metal forming process—II, application of shape optimization in forging. *International Journal for Numerical Methods in Engineering* 1996; **39**:51–65.
5. Chenot JL, Massoni E, Fourment L. Inverse problems in finite element simulation of metal forming processes. *Engineering Computations* 1996; **13**:190–225.
6. Zhao G, Wright E, Grandhi RV. Sensitivity analysis based preform die shape design for net-shape forming. *International Journal of Machine Tools and Manufacture* 1997; **37**:1251–1271.
7. Zhao G, Wright E, Grandhi RV. Preform die shape design in metal forming using an optimization method. *International Journal for Numerical Methods in Engineering* 1997; **40**:1213–1230.
8. Kleiber M. Shape and non-shape structural sensitivity analysis for problems with any material and kinematic non-linearity. *Computer Methods in Applied Mechanics and Engineering* 1993; **108**:73–97.
9. Antunez HJ, Kleiber M. Sensitivity of forming processes to shape parameters. *Computer Methods in Applied Mechanics and Engineering* 1996; **137**:395–409.
10. Joun MS, Hwang SM. Die shape optimal design in three-dimensional shape metal extrusion by the finite element method. *International Journal for Numerical Methods in Engineering* 1998; **41**:311–335.
11. Cao J, Boyce M. A predictive tool for delaying wrinkling and tearing failure in cup forming. *Journal of Engineering Materials and Technology* 1997; **119**:354–365.
12. Jimma T. Deep drawing convex polygon shell researches on the deep drawing of sheet metal by the slip line theory 1st report. *Japan Society of Technology for Plasticity* 1970; **11**:653–670.
13. Hazek VV, Lange K. Use of slip line field method in deep drawing of large irregular shaped components. *Proceedings of the Seventh NAMRC*, SME, Ann Arbor, MI, 1979; 65–71.
14. Karima M. Blank development and tooling design for drawn parts using a modified slip line field based approach. *ASME Journal of Engineering for Industry* 1989; **111**:345–350.
15. Vogel JH, Lee D. An analysis method for deep drawing process design. *International Journal of Mechanical Sciences* 1990; **32**:891–907.
16. Chen X, Sowerby R. The development of ideal blank shapes by the method of plane stress characteristics. *International Journal of Mechanical Sciences* 1992; **34**:159–166.
17. Sowerby R, Duncan JL, Chu E. The modeling of sheet metal stamping. *International Journal of Mechanical Sciences* 1986; **28**:415–430.
18. Blount GN, Stevens PR. Blank shape analysis for heavy gauge metal forming. *Journal of Materials Processing Technology* 1990; **24**:65–74.
19. Tikhonov AN, Arsenin VY. *Solution of Ill-Posed Problems*. V.H. Winston: Washington, DC, 1977.
20. Levy S, Shinh CF, Wilkinson JPD, Stine P, McWilson RC. Analysis of sheet metal forming to axisymmetric shapes. *Formability Topics-Metallic Materials*, Niemeier BA, Schmieder AK, Newby JR (eds). STP, vol. 647, ASTM, 1978; 238–260.
21. Majlessi SA, Lee D. Deep drawing of square-shaped sheet metal parts, Part 1: finite element analysis. *ASME Journal of Engineering for Industry* 1993; **115**:102–109.
22. Guo YQ, Batoz JL, Detraux JM, Duroux P. Finite element procedures for strain estimations of sheet metal forming parts. *International Journal for Numerical Methods in Engineering* 1990; **30**:1385–1401.
23. Chung K, Richmond O. Ideal forming-I. homogeneous deformation with minimum plastic work. *International Journal of Mechanical Sciences* 1992; **34**:575–591.
24. Chung K, Richmond O. Ideal forming-II. sheet forming with optimum deformation. *International Journal of Mechanical Sciences* 1992; **34**:617–633.
25. Chung K, Barlat F, Brem JC, Lege DJ, Richmond O. Blank shape design for a planar anisotropic sheet based on ideal forming design theory and FEM analysis. *International Journal of Mechanical Sciences* 1997; **39**:105–120.
26. Liu SD, Karima M. A one step finite element approach for production design of sheet metal stampings. In *Proceedings of the International Conference on NUMIFORM'92*, Chenot JL, Wood RD, Zienkiewicz OC (eds). Balkema: Valbonne, France, 1992; 497–502.
27. Liu SD, Assempoor A. Development of FAST_3D—a design oriented one step FEM in sheet metal forming. In *Proceedings of the International Conference on Computational Plasticity*. Owen DRJ, Oñate E (eds). CIMNE: Barcelona, Spain, 1995; 1515–1526.
28. Lee CH, Huh H. Estimation of shape and non-shape parameters of sheet metal forming processes with inverse finite element analysis. In *Proceedings of the International Conference on NUMIFORM'98*, Huetink J, Baaijens FPT (eds). Balkema: Enschede, Netherlands, 1998; 793–799.

29. Majlessi SA, Lee D. Development of multistage sheet metal forming analysis method. *Journal of Materials Shaping Technology* 1988; **6**:41–54.
30. Lee CH, Huh H. Three dimensional multi-step inverse analysis for the optimum blank design in sheet metal forming processes. *Journal of Materials Processing Technology* 1998; **80**:76–82.
31. Batoz JL, Guo YQ, Mercier F. The inverse approach including bending effects for the analysis and design of sheet metal forming parts. In *Proceedings of the International Conference on NUMIFORM'95*, Shen SF, Dawson PR (eds). Balkema: Ithaca, NY, 1995; 661–667.
32. Batoz JL, Guo YQ. Analysis and design of sheet forming parts using a simplified inverse approach. In *Proceedings of the International Conference on Computational Plasticity*. Owen DRJ, Onate E, Hinton E (eds). CIMNE: Barcelona, Spain, 1997; 178–195.
33. Stolarski H, Belytschko T, Lee SH. A review of shell elements and corotational theories. *Computational Mechanics Advances* 1995; **2**:125–212.
34. Yang Henry TY, Saigal S, Masud A, Kapania RK. A survey of recent shell finite elements. *International Journal for Numerical Methods in Engineering* 2000; **47**:101–127.
35. Budiansky B, Sanders JL. On the 'Best' first-order linear shell theory. *Progress in Applied Mechanics*, The Prager Anniversary Volume. Macmillan: London, 1963; 129–140.
36. Rodal JJA, Witmer EA. Finite-strain large-deflection elastic-viscoplastic finite-element transient response analysis of structures. *NASA Contractor Report 159874*, NASA Lewis, 1979.
37. ABAQUS Theory Manual Version 5.7. Pawtucket, RI, 1997; 3.6.2-1–3.6.2-10.
38. Hughes TJR, Taylor RL, Kanoknukulchai W. A simple and efficient element for plate bending. *International Journal for Numerical Methods in Engineering* 1997; **11**:1529–1543.
39. Oñate E, Kleiber M, Agelet De Saracibar C. Plastic and viscoplastic flow of void-containing metals. Application to axisymmetric sheet forming problems. *International Journal for Numerical Methods in Engineering* 1988; **25**:227–251.
40. Stanley GM. Continuum-based shell elements. *Ph.D. Dissertation*, Applied Mechanics Division, Stanford University, CA, 1985.
41. Chung K, Richmond O. Sheet forming process design based on ideal forming Theory. In *Proceedings of the International Conference on NUMIFORM'92*, Chenot JL, Wood RD, Zienkiewicz OC (eds). Balkema: Valbonne, France, 1992, 455–460.
42. ABAQUS user's manual Version 5.7. Pawtucket, RI, 1997; 15.5.5-1–15.5.5-9.
43. Oñate E, Zienkiewicz OC. A viscous shell formulation for the analysis of thin sheet metal forming. *International Journal of Mechanical Sciences* 1983; **25**:305–335.
44. ABAQUS example manual Version 5.7. Pawtucket, RI, 1997; 4.2.16-1–4.2.16-21.